

Design of an Adaptive Shock Control Bump using Pressurized Chambers

Structural Realization, Actuation and Integration

Nuno Borges Loureiro Alves de Sousa
nunoalvesdesousa@tecnico.ulisboa.pt

Instituto Superior Técnico, Universidade de Lisboa, Portugal

June 2017

Abstract

The dawn of research on shock and boundary layer interaction control dates back to the 1970's, when humped transonic aerofoils were first studied as a means to improve the performance of supercritical aerofoil technology at off-design conditions. Since then, shock control bumps (SCBs) have been found to be promising devices for such kind of flow control. They have a smearing effect on the shock wave structure achieved through isentropic pre-compression of the flow upstream of the main shock and can significantly lower wave drag without incurring unacceptable viscous losses. However, their performance is strongly dependent on a set of geometrical parameters which must be adjusted according to the ever-changing flight conditions.

A concept for an adaptive SCB is therefore presented. The proposed actuation mechanism aims at a compact, lightweight and simple structure which could be integrated into the spoiler region of near-future aircraft without major design changes required. Numerical optimization of a simplified analytical model of the structure is used to investigate the SCB adaptation to various aerodynamic target shapes. Compromises between geometrical conformity and both structural and actuation related requirements are studied. Furthermore, an outlook is given on design issues related to three-dimensional effects on a finite span SCB.

Keywords: shock control bump; wave drag minimization; morphing spoiler; pressure actuated adaptive structure; structural optimization.

1. Introduction

Aircraft manufacturers are aware that even small efficiency gains can represent substantial savings for air operators in the ever more competitive air transport sector. Therefore, modern aircraft technologies are focusing on the reduction of direct operating costs (DOCs) and increase in mission flexibility as a means to achieve a competitive advantage. Most of high economic and industrial impact technologies are dependent on the optimization of the aerodynamic efficiency of the main wing which has long been an area of design compromises for the engineer: a narrower cruise envelope leads to higher efficiency gains with worse off-design performance, while a wider cruise envelope means less efficiency gains within the operating conditions.

Large scale morphing technologies dealing with the adaptation of the entire wing as described by Smith et al. [7] ensure that each operating point is a design optimum. Nevertheless, this approach requires complex actuation mechanisms and can be seen as a long-term solution. A more feasible approach would be adapting the aerofoil geometry by focusing on individual movable parts *i.e.* leading edge, flaps and spoiler devices. In fact, the EU-

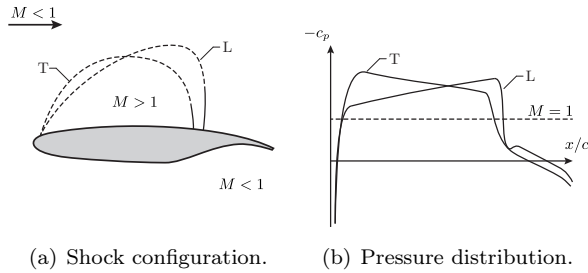
ROSHOCK I & II programs [4, 9] showed that the use of a physical bump in order to adapt a relatively small portion of the suction side of the main wing, as initially proposed by Ashill et al. [1], is an effective way of minimizing wave drag due to the strong shock waves that develop at transonic cruise conditions. Thereafter, the so-called shock control bump (SCB) has been subject to various aerodynamic investigations and its role as a flow control device is becoming increasingly popular.

This study focuses on the structural realization and actuation of such devices. It is therefore useful to first introduce basic aerodynamic principles regarding SCBs in order to understand how they relate to structural constraints.

2. Aerodynamic Principles

Increasing the free-stream Mach number (M_∞) or angle of incidence (lift) of a transonic aerofoil will lead to the development of a supersonic region on the upper surface. For a modern turbulent design, the supersonic flow will usually be terminated by an isentropic recompression or a weak shock wave as shown in fig. 1 (T). If either free-stream parameter is increased, commonly the shock will strengthen leading to extra wave drag culminating in separa-

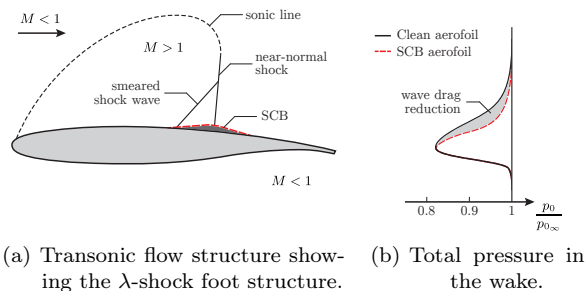
tion which defines the drag-rise and buffet boundaries. For a laminar aerofoil - fig. 1 (L) - the flow undergoes a continuous acceleration on the upper surface causing stronger shock waves, even for the design conditions.



(a) Shock configuration. (b) Pressure distribution.
Figure 1: Transonic flow for a turbulent (T) and a laminar (L) aerofoil at equal lift.

Across the shock entropy increases and total pressure decreases. Wave drag is then generated and it seriously limits cruise efficiency of current aircraft configurations.

SCBs can split the stronger single shock into a series of weaker oblique shocks or compression waves that decelerate the flow more isentropically than the uncontrolled shock wave. The result is a reduced stagnation pressure loss across the shock leading to lower drag. Fig. 2 illustrates the principle of operation of SCBs in transonic flight.



(a) Transonic flow structure showing the λ -shock foot structure. (b) Total pressure in the wake.
Figure 2: Principle of operation of a SCB on a supercritical wing.

SCB geometry is usually comprised of a ramp upstream of the nominal shock position, a short crest region and a tail. The function of the ramp is to generate an oblique shock or multiple oblique compression waves ahead of the main shock deflecting the incoming supersonic flow away from the surface. Close to the crest, a near-normal shock decelerates the flow to subsonic velocities. The tail then brings the post-shock flow back to the aerofoil surface.

SCBs can be classified as: two-dimensional (2D) SCBs - a constant profile along the wing span; and three-dimensional (3D) SCBs - a series of short-width bumps distributed along the wing. This work will focus on 2D SCBs as they present the highest potential for efficiency gains.

Fig. 3 summarizes the characteristic geometric parameters of a SCB: the bump is located on an aerofoil surface of chord c at a position x_0 from the leading edge. It has a crest of length c_B and

height h_B , which is schematically represented by point $C(c_B, h_B)$. The bump is also defined by its length l_B and its shape f_B .

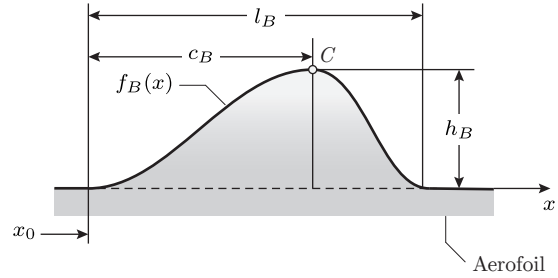


Figure 3: Definition of characteristic geometric parameters for 2D SCBs.

Table 1 shows reference ranges considered by a multitude of aerodynamic studies on SCBs. A significant aspect to retain is the fact that SCB research has essentially focused on bumps with heights of the order of the local boundary layer thickness. Additionally, typical peak shock strength is around $M = 1.3 \pm 0.2$.

Symbol	Parameter	Typical values
h_B	SCB height	$\delta_0 \pm \delta_0$
l_B	SCB length	$\frac{l_B}{c} \in [12\%; 20\%]$
c_B	Crest length	$\frac{c_B}{l_B} \in [30\%; 80\%]$

Table 1: Characteristic SCB parameters and typical values investigated.

2.1. Aerodynamic Performance of SCBs

Previous works by Dargel et al. [3] and Sommerer et al. [8] have shown that the drag reduction potential of SCBs depends strongly on the correct bump position, height and location of the bump maximum. The bump height depends on the actual flight conditions and the aerofoil geometry, but can be estimated to be within 0.5 percent of the local chord length. An interesting result from these investigations is the fact that the detailed bump shape does not have a strong effect on the bump effectiveness.

Fig. 4 is helpful in understanding why the bump position, height and location of the bump maximum play a major role in SCB performance. When the shock is at the optimum location - fig. 4(b) - a "cleaner pressure" rise has the least negative effect on the boundary layer. The off-design cases - fig. 4(a) and (c) - introduce a re-expansion and secondary shock structures which significantly impact the incoming boundary layer: when the shock is upstream of the optimum location, the bump accelerates the flow forming a secondary shock - fig. 4(a); when the shock is downstream of the optimum location, there is an unfavourable expansion over the bump

crest leading to a stronger shock and ultimately to boundary layer separation - fig. 4(c).

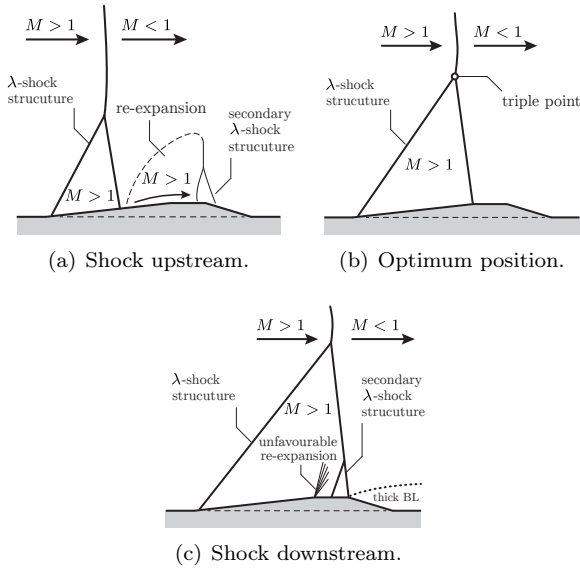


Figure 4: Impact of shock position on the flow structure generated by a straight ramp, straight tail SCB.

As a consequence, static SCBs present a narrow region of effectiveness. When the flight conditions lead to non-optimum shock locations SCB performance is worse than that of a clean aerofoil. Since there is some shock mobility during cruise, it is essential to be able to continuously adapt the significant SCB parameters according to the actual shock position. This sets the case for an adaptive SCB, where the main actuation objective is the ability to adjust the crest position.

3. Structural Concept, Model and Optimization

While there are numerous publications dealing with the aerodynamic design of SCBs, the structural realization of such a structure-system is still a key challenge. For current transport aircraft, even though during flight shock movement is always an obstacle, the shock location is generally restricted to the rear portion of the wing, *i.e.* the region closer to the spoilers and the wing trailing edge. In order to allow an easy integration of SCBs in near-future transport aircraft, the proposed system location is the spoiler region. The available design space is therefore extremely limited and the main drivers for concept selection should be: a compact design, lightweight structure and low complexity actuation mechanism for the SCB deployment.

3.1. Concept

The main design objective is to achieve a structure capable of conforming to prescribed optimal aerodynamic bump shapes (or at least a set of crest positions) while having enough structural stiffness in order to resist aerodynamic loads. Therefore, a new integral spoiler structure has been selected.

The new integral spoiler structure is comprised of three layers: the top layer is an active surface where the SCB is generated, the bottom layer is a load-carrying structure which supports both aerodynamic loads and actuation loads for the SCB and the middle layer is where the internal actuation mechanism for the SCB deployment is fitted. This approach does not require a complete redesign of the spoiler deployment mechanism since the actuation of the SCB is independent of the spoiler deployment mechanism. The passive structure greatly simplifies the design of the SCB actuation system as it provides the necessary support for the actuation loads.

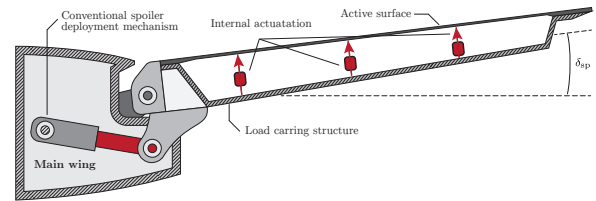


Figure 5: The integral spoiler structure.

This design approach separates the functional (active) structure from the supporting structure thanks to a mechanical parallel actuation system as Wadehn et al. [10] and Bein et al. [2] proposed. These authors also proposed the use shape-memory alloy (SMA) actuated deformation and pressurized tube springs as variations on the linear actuator for internal actuation. However, this approach requires the use of numerous actuators.

A spoiler concept using pressurized chambers was selected as a pioneering actuation technology that is able to combine the key requirements. The SCB deployment and its adaptation to the changing flight conditions is realized by differential pressurization of chambers inside the spoiler body, as shown in fig. 6. A series of chambers could be combined into one single part during manufacturing. This reduces the actuation mechanism to a sealed assembly that can easily be replaced in case of a repair. The chambers are supported by the conventional load-carrying structure and spanwise stiffeners can be designed according to the needs of the parallel actuation system using stringers embedded into the interfaces (chamber walls) between each chamber. Therefore, the cross-sectional stringer shape must be designed to allow deformation in the direction of the chamber height while at the same time providing spanwise support. Since pressure acts uniformly across the entire span of the spoiler, spanwise waviness issues are not expected. Moreover, the elastomeric material of the chamber walls allows for a compact and lightweight mechanism. Finally, since pressure is allowed to act on the entire portion of the flexible skin that contacts each chamber, it is predictable that the number of chambers, *i.e.* actu-

ators, might be reduced when compared to previous concepts, also contributing to a more compact and lightweight structure.

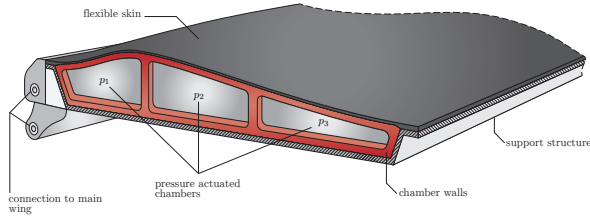


Figure 6: Spoiler concept with pressurized chambers for an adaptive SCB.

3.2. Analytical Model

A design tool was developed to provide a systematic way of investigating key structural and functional interdependencies related to the actuation of the selected design concept. This tool aims to provide the foundations for an accurate sizing of the functional layer of the SCB and give an insight on the trade-offs between structural integrity and geometrical conformity qualities that the engineer will face. The simplified analytical model used by the design tool is now presented.

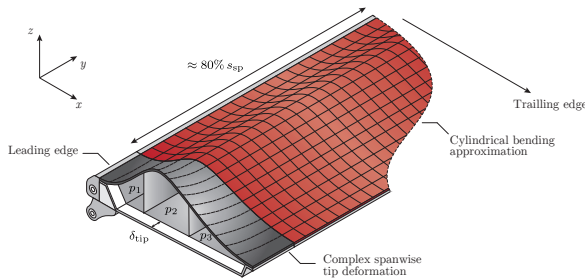


Figure 7: Simplified structural model showing typical deformation regions of the active surface.

Fig. 7 shows the simplified spoiler model where the x and y coordinate directions are the chordwise and spanwise directions, respectively. The upper spoiler skin is modelled as a transversely loaded plate while the main lower body is assumed to be comparably much stiffer. The upper skin is clamped to the support structure and free at the spoiler tips. Given that the considered SCB height to length ratios are below 5%, small strains and moderate rotations are expected. For this reason, the Kirchhoff plate theory will be used. For transversely loaded Kirchhoff plates, the static bending equation is

$$D_{11} \frac{\partial^4 w_0}{\partial x^4} + 2(D_{12} + 2D_{66}) \frac{\partial^4 w_0}{\partial x^2 \partial y^2} + D_{22} \frac{\partial^4 w_0}{\partial y^4} = q(x, y), \quad (1)$$

where w_0 is the transverse displacement of a point on the plate midplane, D_{ij} are the *bending stiff-*

nesses and q is the distributed transverse loading. Considering a reference frame centred at the spoiler leading edge, the boundary conditions for the clamped edges are given by

$$\Gamma_u : w_0 = 0, \quad \left. \frac{\partial w_0}{\partial n} \right|_{n=x} = 0, \quad x = \{0, l_B\}; \quad (2)$$

where Γ_u indicates essential boundary conditions, n is the direction normal to the clamped edge and l_B is the bump length. For the free-edges, natural boundary conditions are defined using the bending moment M_{nn} and the Kirchhoff free-edge condition:

$$\Gamma_\sigma : M_{nn} = 0, \quad V_n \equiv Q_n + \frac{\partial M_{ns}}{\partial s} = 0, \quad y = \pm \frac{s_{sp}}{2}; \quad (3)$$

where V_n is the total vertical force given in terms of the vertical resultant Q_n and moment M_{ns} and s_{sp} is the spoiler span. The first index represents the normal direction to the edge surface. For the moments, the second index is the direction along which the force causing the moment is acting. Once more, n is the normal to the free-edge, *i.e.* \hat{e}_y and s is the tangent direction to the free edge *i.e.* \hat{e}_x .

The materials investigated will be restricted to single layer specially orthotropic and isotropic laminates. For these cases, the bending stiffnesses, vertical resultant and moments can be written in terms of the lamina engineering constants and equation 1 can be recasted into:

$$\frac{\partial^4 w_0}{\partial x^4} + 2 \left[\nu_{21} + 2 \frac{G_{12}}{E_1} (1 - \nu_{12} \nu_{21}) \right] \frac{\partial^4 w_0}{\partial x^2 \partial y^2} + \frac{\nu_{21}}{\nu_{12}} \frac{\partial^4 w_0}{\partial y^4} = \frac{q}{\hat{D}}, \quad \hat{D} \equiv \frac{E_1 h^3}{12(1 - \nu_{12} \nu_{21})}; \quad (4)$$

where h is the laminate thickness. The boundary conditions, can also be written in terms of the displacement w_0 . For the natural boundary conditions, laminate constitutive equations for specially orthotropic materials have been used to resolve the forces and moments in equation 3 into the displacement w_0 :

$$\Gamma_u : w_0 = 0, \quad \frac{\partial w_0}{\partial x} = 0, \quad x = \{0, l_B\}; \quad \Gamma_\sigma : \nu_{12} \frac{\partial^2 w_0}{\partial x^2} + \frac{\partial^2 w_0}{\partial y^2} = 0, \quad \left(\nu_{12} + 4 \frac{G_{12}}{E_2} (1 - \nu_{12} \nu_{21}) \right) \frac{\partial^3 w_0}{\partial x^2 \partial y} + \frac{\partial^3 w_0}{\partial y^3} = 0, \quad y = \pm \frac{s_{sp}}{2}. \quad (5)$$

The problem requires approximate analytical solution methods like the Ritz method or numerical methods like the FEM. However, if the SCB span

to length ratio is large enough, and assuming that the pressurization of the chambers is sufficiently uniform, $y \gg x$ and $q \approx q(x)$. Under these circumstances, the central portion of the active layer behaves as a long semi-infinite plate strip and the cylindrical bending approximation greatly simplifies the solution of equation 4 by reducing the problem to one dimension. The $\partial/\partial y$ derivatives vanish and the natural boundary conditions are eliminated, which means $w_0 = w_0(x)$. The governing equation and boundary conditions are simply:

$$\frac{d^4 w_0}{dx^4} = \frac{q}{\hat{D}} \quad , \quad \hat{D} \equiv \frac{E_1 h^3}{12(1 - \nu_{12}\nu_{21})}; \quad (6)$$

$$\Gamma_u : w_0 = 0 \quad , \quad \frac{dw_0}{dx} = 0 \quad , \quad x = \{0, l_B\}. \quad (7)$$

One should note the similarity between equation 6 and the classical beam bending equation. The difference is in the bending stiffness under cylindrical bending which includes the Poisson's ratios due to the plane strain assumption. Figure 7 also shows the area where the cylindrical bending approximation is valid in red.

For the SCBs investigated within the LDAinOp program the SCB span to length ratio, *i.e.* aspect ratio (\mathcal{R}), is often larger than seven. Even for lower aspect ratio SCBs located in the inner region of the main wing ($\mathcal{R} > 2.5$) the approximation is reasonable for approximately 80% of the SCB span. In the outer region near the spoiler tips there is a complex spanwise deformation.

Fig. 8 shows the effect of SCB aspect ratio on the spanwise deformation of the SCB crest (located at $x = c_B = l_B/2$) in terms of the dimensionless spanwise coordinate $\tilde{y} = y/s_{sp}$. Each curve is associated with a different aspect ratio for the chosen pressurization. The topology of the spanwise deformation at other chordwise positions of the active layer is similar to that shown in fig. 8 although the deflections involved are smaller.

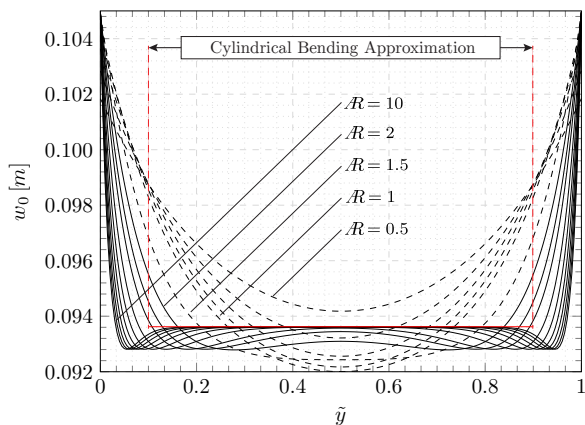


Figure 8: Effect of SCB aspect ratio on the spanwise deformation of the bump crest located at $x = l_B/2$.

As the aspect ratio increases, a region of uniform

spanwise deformation appears. The deflection is accurately predicted by the aforementioned approximation. Fig. 9 shows the the relative difference between the deflection of the half span crest and the cylindrical bending approximation (solid line). Due to the linearity of equation 6, the results are similar for different pressurization levels as shown.

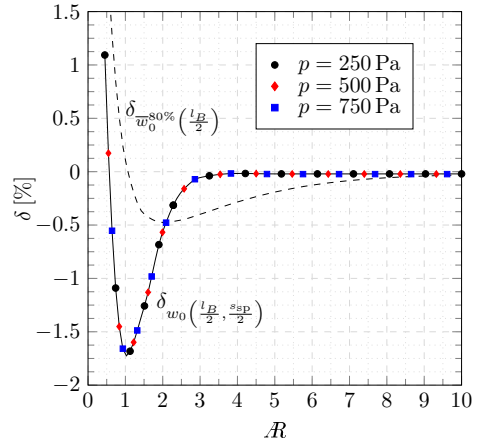


Figure 9: \mathcal{R} effect on the half-span crest and 80%-span mean deflection for different pressurizations.

The dashed line represents the relative difference between the mean deflection of 80% of the spoiler span and the cylindrical bending approximation. In both cases, for $\mathcal{R} > 2$ the error of the approximation remains below 0.5% and for that reason it was deemed an adequate simplification that allows an efficient structural solver and avoids a full plate model.

3.3. Structural Module

A structural module was developed based on the analytic element method (AEM) approach as described by Policarpo et al. [6]. This allows for a structural solver which is both accurate and efficient. The module is then used in an optimization environment where the desired bump shapes are fed to the optimization algorithm through an objective function as target shapes in order to find the optimized design parameters that minimize the difference between the target shape (*i.e.* the desired aerodynamic bump shape) and the optimized shape.

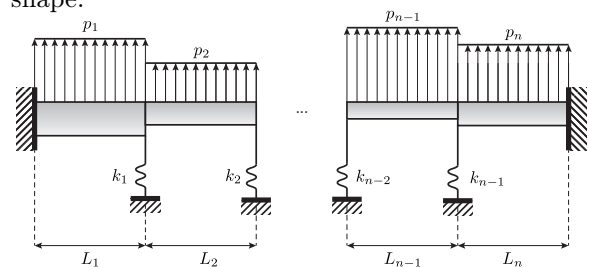


Figure 10: Simplified 2D model used in the structural module.

Fig. 10 shows the active surface of the SCB idealized as a series of plate strips spanning along the

y direction which are actuated by the pressurized chambers inside the spoiler body. A spring is used to model the stiffness of the interface between consecutive chambers whose pressure is kept uniform.

As a first approach, the pressurization of each chamber will be assumed uniform in the spanwise and chordwise directions. The deflection of a point in the midplane of the plate strip actuated by the i^{th} chamber is obtained from equation 6:

$$w_{0_i}(x) = \frac{p_i}{24\hat{D}_i}x^4 + C_1^i x^3 + C_2^i x^2 + C_3^i x + C_4^i, \quad (8)$$

where \hat{D}_i is the bending stiffness of the i^{th} plate strip and C^i are the set of constants to be determined using the boundary conditions. Fig. 11 shows an element of plate strip under cylindrical bending and the sign convention for the transverse force (Q_x) and bending moment (M_{xx}), as well as for the nodal degrees of freedom (DoFs) (*i.e.* the nodal deflections and rotations).

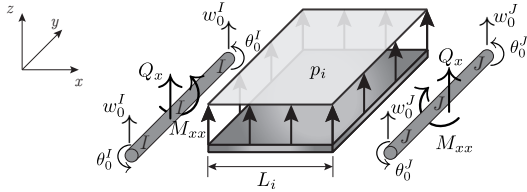


Figure 11: Schematic representation of a plate strip element.

Using the definitions of the transverse force Q_x and bending moment M_{xx} , and the strain-displacement relations, the loads on the left (I), and right (J) nodes of the i^{th} plate strip can then be related the C^i analytic constants:

$$\begin{Bmatrix} F^I \\ M^I \\ F^J \\ M^J \end{Bmatrix}_i = \begin{Bmatrix} -Q_x(x_i = 0) \\ M_{xx}(x_i = 0) \\ Q_x(x_i = L_i) \\ -M_{xx}(x_i = L_i) \end{Bmatrix}_i = \hat{D} \begin{Bmatrix} \frac{\partial^3 w_0}{\partial x^3} \\ -\frac{\partial^2 w_0}{\partial x^2} \\ -\frac{\partial w_0}{\partial x} \\ w_0 \end{Bmatrix}_i. \quad (9)$$

And using equation 8:

$$\begin{Bmatrix} F^I \\ M^I \\ F^J \\ M^J \end{Bmatrix}_i = \hat{D}_i \underbrace{\begin{bmatrix} 6 & 0 & 0 & 0 \\ 0 & -2 & 0 & 0 \\ -6 & 0 & 0 & 0 \\ 6L_i & 2L_i & 0 & 0 \end{bmatrix}}_{[B]} \underbrace{\begin{Bmatrix} C_1^i \\ C_2^i \\ C_3^i \\ C_4^i \end{Bmatrix}}_{\{c\}} + p_i \underbrace{\begin{Bmatrix} 0 \\ 0 \\ -L_i \\ \frac{L_i^2}{2} \end{Bmatrix}}_{\{g\}}. \quad (10)$$

It is also possible to relate the nodal DoFs to the

C^i constants. Noting that $\theta_0(x) = \frac{dw_0}{dx}$:

$$\underbrace{\begin{Bmatrix} w_0^I \\ \theta_0^I \\ w_0^J \\ \theta_0^J \end{Bmatrix}}_{\{p\}}_i = \begin{Bmatrix} w_0(x_i = 0) \\ w_0'(x_i = 0) \\ w_0(x_i = L_i) \\ w_0'(x_i = L_i) \end{Bmatrix}_i = \underbrace{\begin{bmatrix} 0 & 0 & 0 & 1 \\ 0 & 0 & 1 & 0 \\ L_i^3 & L_i^2 & L_i & 1 \\ 3L_i^2 & 2L_i & 1 & 0 \end{bmatrix}}_{[C]} \underbrace{\begin{Bmatrix} C_1^i \\ C_2^i \\ C_3^i \\ C_4^i \end{Bmatrix}}_{\{c\}} + p_i \underbrace{\begin{Bmatrix} 0 \\ 0 \\ \frac{L_i^4}{24\hat{D}_i} \\ \frac{L_i^3}{6\hat{D}_i} \end{Bmatrix}}_{\{g\}}. \quad (11)$$

Equations 10 and 11 can be written in compact form as follows:

$$\{F\} = [B]\{c\} + \{g\} \quad (12)$$

$$\{p\} = [C]\{c\} + \{g\}, \quad (13)$$

where $\{F\}$ is the vector of nodal forces, $\{p\}$ is the vector of nodal DoFs and $\{c\}$ is the vector containing the C^i analytic constants. Solving equation 13 for $\{c\}$ and introducing into equation 12 yields a familiar FEM-like representation:

$$[K]\{p\} = \{F\} + \{f\}, \quad (14)$$

where $[K]$ is the stiffness matrix and $\{f\}$ is the vector of distributed loads. Again, there is a resemblance between the AEM equation for a plate strip element under cylindrical bending and the finite element method (FEM) equation of a classical beam element. The relation with the original matrices is given by

$$[K] = [B][C]^{-1}\{p\} \quad (15)$$

$$\{f\} = ([B][C]^{-1} - [I])\{g\}, \quad (16)$$

where $[I]$ is the 4×4 identity matrix. Given the parallelism between the AEM and FEM approaches, the AEM solver implementation is indeed akin to that of the FEM for the algorithms of assembly and solving of the global system of equations. However, once the global system of equations has been solved and the nodal DoFs have been element-wise reconstructed, finding the deflection w_{0_i} requires computing the analytic constants by solving equation 13 for $\{c\}$. On the other hand, the FEM requires a linear combination of shape functions using each element's nodal DoFs as scalar coefficients.

3.4. Optimization Module

The optimization module uses the Nelder-Mead simplex direct search method [5] and includes variable transformation to address bound constraints for the optimization parameters. This can be used to define both design criteria constraints (*e.g.*: minimum active layer thickness and chamber length) as

well as constraints imposed by pressure limits inside each chamber. The design parameters include:

- α_i - the relative position of each chamber interface as a percentage of the total spoiler chord;
- h_i - the thickness of the upper skin (active layer) of each chamber;
- k_i - the spring constant modelling the stiffness of the chamber interface;
- p_i - the actuation pressure in each chamber.

Fig. 12 shows how the structural and optimization modules are integrated into the design tool algorithm.

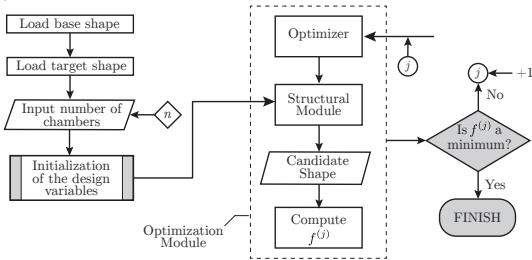


Figure 12: Flow diagram for the design tool algorithm.

The base and target shapes are first loaded and the user inputs the number of pressurized chambers. Each chamber is associated with a series of new optimization parameters. Adding chambers has therefore a very significant impact on the problem complexity. Moreover, increasing the number of optimization parameters has a disproportional effect on the number of calculations the optimization algorithm must perform and consequently leads to a rapid growth of the algorithm runtime.

The value $f^{(j)}$ refers to the objective function value at the end of the j^{th} iteration.

4. Bi-Dimensional Design

The adaptability characteristics of the proposed spoiler concept are now analysed. An uncurved 5 mm thick functional skin made of GFRP has been selected as the baseline geometry and the span is 10 m. The actuation mechanism is based on a two chamber spoiler design in order to determine if a compromise between design complexity and adaptability qualities can be struck without resorting to additional chambers.

The position and stiffness of the chamber interface, play an important role on the achievable geometrical conformity. However, they are not actuation variables but variables of the structural design which must be fixed once the spoiler structure is derived.

As a feasibility demonstration, the adaptability analysis is based on a worst-case scenario: as the crest position moves towards the leading and trailing edges, the required stiffness of the chamber interface increases abruptly. However, for symmetrical bumps, it is null. Therefore, setting the de-

sign point of the spoiler to $(c_B)_{\text{design}} = \frac{l_B}{2}$ is specially challenging in terms of extended adaptability over a large range of crest lengths. This also requires setting the position of the chamber interface to $(\alpha_1)_{\text{design}} = 0.5$. The stiffness of the chamber interface can be determined by defining an actuation limit $(c_B)_{\text{lim}}$ and then, using the design tool, compute $(k_1)_{\text{design}}$ that, subject to $(\alpha_1)_{\text{design}} = 0.5$, offers the best geometrical conformity for the actuation limit $c_{B_{\text{lim}}}$. In keeping with the worst-case scenario approach, a narrow actuation limit of $c_{B_{\text{lim}}} = 0.425$ m was chosen which leads to $(k_1)_{\text{design}} = k_1(c_B = 0.425)|_{\alpha=0.5} \approx 1.7 \times 10^5$ N/m.

4.1. Deformation Envelope

Fig. 13 shows a series of target shapes (in red) containing a set of crest lengths c_B . The effective range of crest lengths is actually double, since results on the rear portion of the spoiler are analogous and have been omitted for conciseness. The design tool was used to determine the best morph of the active layer to each of the target shapes using the actuation pressures (p_1, p_2) subject to $(\alpha_1)_{\text{design}} = 0.5$ and $(k_1)_{\text{design}} \approx 1.7 \times 10^5$ N/m. The set of optimized shapes (in black) forms a *deformation envelope* which represents the manifold of educible morphs. The actuation limits are revealed when an increased chamber pressurization is unable to move the crest position closer to the leading edge, but instead causes the bump height to increase.

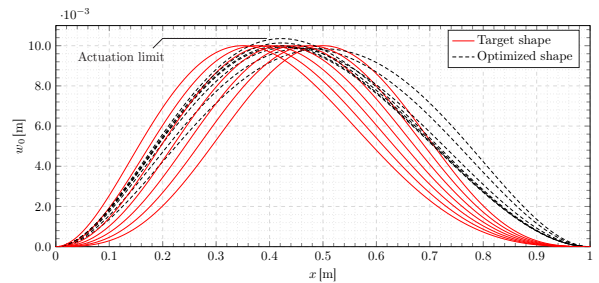


Figure 13: Deformation envelope after fixing $(\alpha_1)_{\text{design}}$ and $(k_1)_{\text{design}}$.

4.2. Actuation Characteristics

The relation between the deformation envelope and the actuation pressure is shown in fig. 14. Since the actuation mechanism is driven by the chamber pressures, the envelope of these variables will be referred to as the *actuation envelope*.

The actuation envelope shows that the minimum actuation pressure occurs for $c_B = 0.5$ m when the left (p_1) and right (p_2) chambers are equally pressurized. As the bumps become more asymmetrical, so does the chamber pressurization. This goes on until the right chamber is unpressurized and the actuation limits are reached. This also illustrates how the range of adaptability is limited by the design choices: if adaptability were the design driver,

a lower $(c_B)_{\text{lim}}$. would lead to a stiffer chamber interface, *i.e.* higher $(k_1)_{\text{design}}$, and an increased minimum actuation pressure. The result would be more leeway for asymmetrical pressurization, and therefore, wider actuation limits.

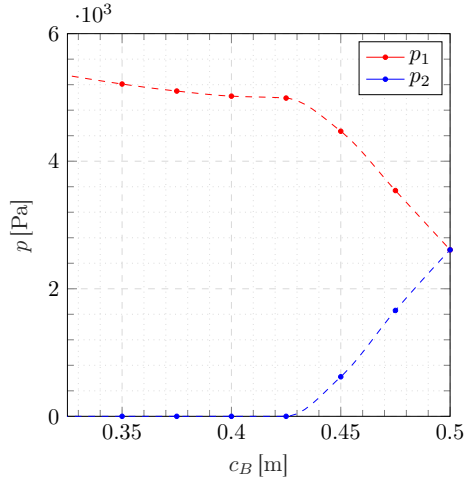


Figure 14: Actuation envelope for the final actuation mechanism.

Fig. 15 shows the envelope of the design objective (f_3) which is a measure of geometrical deviation between target and optimized shapes. The black line shows the initial design space before fixing α_1 and k_1 . The blue line shows the design space after fixing $(\alpha_1)_{\text{design}}$ and, as expected, the geometrical conformity at $(c_B)_{\text{design}} = 0.5$ m is unaffected. However, the design space is reduced and the geometrical conformity for other crest lengths is affected. The final actuation domain is represented by the red line: the geometrical conformity at the design point is now impacted as a drawback for the adaptability range imposed by setting the actuation limits $c_{B_{\text{lim}}}$.

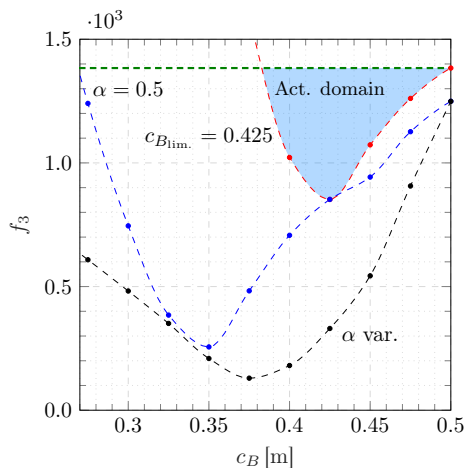


Figure 15: Morph quality for the final actuation mechanism.

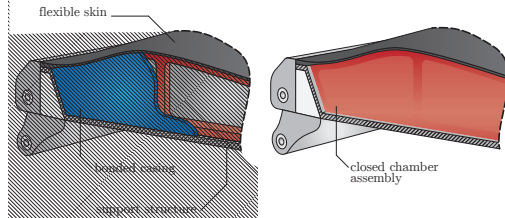
The feasibility study shows that, even for a challenging design scenario, it is possible to achieve an actuation domain of feasible crest lengths that corresponds to over 20% the SCB length.

5. Three-Dimensional Design

The cylindrical bending approximation, even though useful, does not capture the complete three-dimensional behaviour of the spoiler. Important three-dimensional effects are also analysed. The design of the spoiler tips is studied. The effect of tapering is investigated. Finally, a strategy to control tip deformation is presented.

5.1. Spoiler Tip Design

The SCB actuation was reduced to a bi-dimensional problem assuming that the active layer could be modelled as a semi-infinite plate strip. This assumption implied that the spoiler tips were sufficiently separated so that the corresponding boundary conditions did not significantly influence the bending problem. In this section, the effect of different tip designs will be analysed considering two distinct configurations: (A) a spoiler with an exterior casing; and (B) a spoiler with open ends (and thus free tips).



(a) Spoiler with an exterior casing. (b) Spoiler with an independent chamber assembly.

Figure 16: Different designs for the tip region of the spoiler.

Fig. 17 shows the evolution of the deflection of the half-span crest located at $(\frac{l_B}{2}, \frac{s_{SP}}{2})$ and 90%-span mean deflection. The limits on the mean deflection \bar{w}_0^α for the two configurations are shown as shaded areas denoted by $\bar{w}_0^{100\%}$.

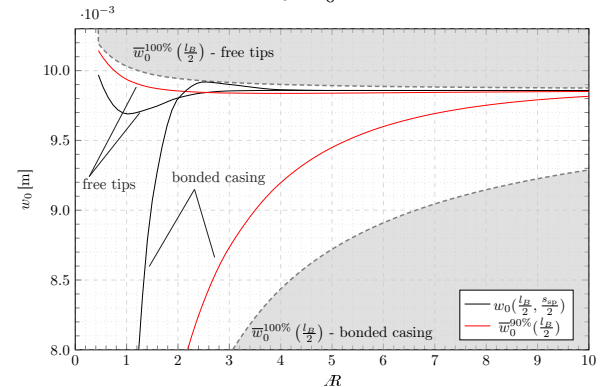


Figure 17: \mathcal{AR} effect on the half-span crest and α -span mean deflections for different tip designs.

The effect of SCB aspect ratio on the bending stiffness of configurations (A) and (B) is illustrated by the opposite evolution of the respective half-span crest deflections (in black) for lower aspect ratios.

For $\mathcal{R} > 4$ the half-span crest reaches the cylindrical bending prediction and both configurations exhibit similar deflections. Although the half-span crests of both configurations eventually reach the same deflection, that is not an indication that they are then aerodynamically equivalent.

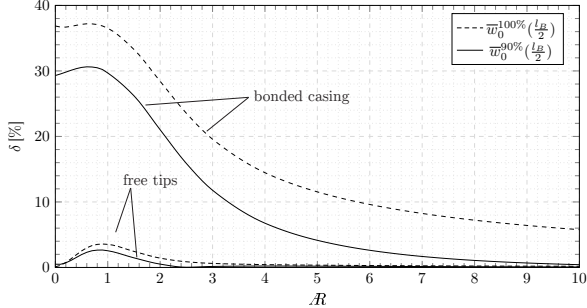


Figure 18: Difference between half-span crest and mean deflections for different tip designs.

Fig. 18 illustrates the relative difference between the deflection of the half-span crest and 90% and 100%-span mean deflections. Indeed both configurations exhibit a maximum for SCBs close to unit aspect ratio. The difference continuously decreases with increasing aspect ratio. Nonetheless, the configuration with a bonded casing converges much slower to a spanwise-uniform bump, hence becoming less aerodynamically efficient than configuration (B) for a given aspect ratio. Moreover, 90% of the spoiler span of the configuration with free tips can be considered to uniformly deploy the functional layer at around $\mathcal{R} = 2$ ($\delta < 1\%$) while a similar efficiency using a bonded casing requires SCBs of aspect ratios between eight and nine. Another relevant limitation of using a bonded casing is the fact that its application to inboard spoilers - which typically present aspect ratios around two or three - can significantly lower the SCB drag reduction potential (between 10% and 20%) when compared to configuration (B). Finally, fig. 17 and 18 show that even for high aspect ratio SCBs - where the two configurations perform similarly across 90% of the spoiler span - using a bonded casing inevitably implies a loss of at least 5% in drag reduction potential due to the external 10% of the spoiler span.

5.2. Tapered SCB

Tapering is another three-dimensional effect that has relevant implications on the actuation mechanism. Tapering ratios as low as 0.5 and 0.8 are under investigation in the LDAinOP project for the outboard and inboard spoilers, respectively. Figure 19 shows the crest deflection for different taper ratios. The spoiler was modelled with free tips.

For moderate taper ratios ($\lambda_{sp} \geq 0.8$) and independently of \mathcal{R} , the spanwise deflection of the crest reduces linearly from the spoiler root ($\tilde{y} = 0$), to the tip ($\tilde{y} = 1$).

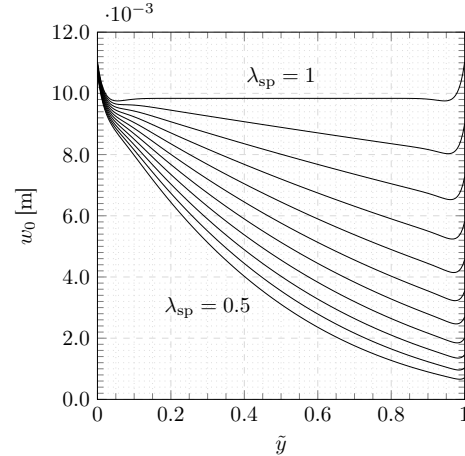


Figure 19: Spanwise crest deflection as a function of taper ratio.

Fig. 20 shows the effect of tapering on the mean crest deflections. Although there is a significant change in deflection of the half-span crest due to tapering, for a given taper ratio, the mean deflection across the entire spoiler span does not deviate significantly.

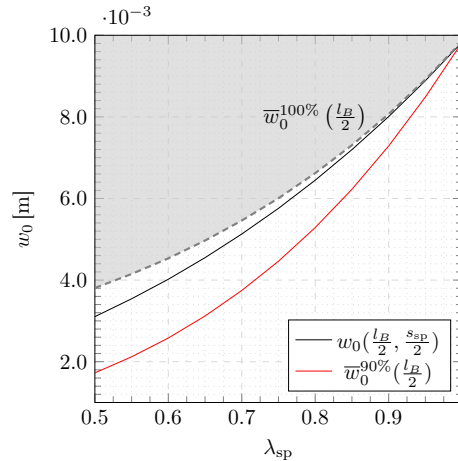


Figure 20: Effect of taper ratio on the mean deflections.

Given this result, it is reasonable to consider that even though the actuation pressure must be corrected in order to account for tapering, this might be achieved by scaling it proportionately to $\bar{w}_0^{100\%}$ and uniformly across the spoiler span. However, figure 20 also shows that, even for low taper ratios, $\bar{w}_0^{90\%}$ deviates considerably from the half-span crest deflection. This means that the functional layer might be on average at a deflection close to that of the half-span crest, but there are however large deflection gradients across its span. Therefore, a uniform correction of the actuation pressure would lead to considerably lower deflections of the spoiler region close to the tips. Conversely, the region closer to the spoiler root would experience significantly larger deflections. While the former situation translates to a lower drag reduction potential, the latter

has more serious consequences: overestimating the bump height not only leads to an accentuated loss of drag reduction potential, but it might even lead to added drag when compared to a clean aerofoil, which would defeat the purpose of having a SCB altogether.

As a consequence, using tapering requires not only correcting the actuation pressure, but as demonstrated, this correction must be done using at least two to three sections of the spoiler span with progressively higher pressurizations.

5.3. Uniformization of Tip Deformation

The behaviour of the non-uniform spanwise deformation near the tip region of the active layer on a spoiler with free tips can be adjusted using only the offset distance introduced in fig. 7. The portion of the tips enclosed by δ_{tip} is unpressurised

Adjusting the offset distance allows the tip deflection to be changed considerably without affecting either the half-span crest or the mean deflection.

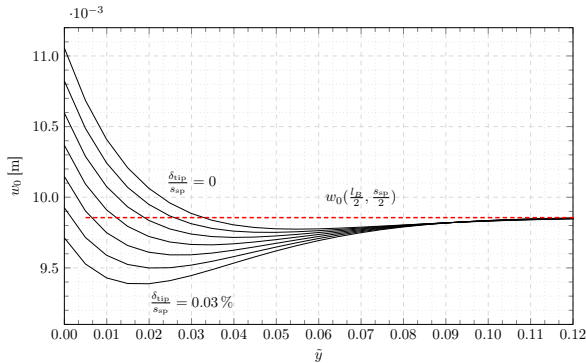


Figure 21: Detailed spanwise deformation of the spoiler tips.

Figure 21 shows the effect of the offset distance on tip deformation. The deflection of the half-span crest is depicted in red as a reference.

Recalling that an overestimation of the bump height can lead not only to lower drag reduction potential, but in the worse case scenario added drag, the offset distance is an important design variable that allows the aerodynamicist to control eventual localized drag penalties in the tip region without resorting to more complex tip designs such as a spoiler with a bonded casing.

6. Concluding Remarks

Taking into account that the successful implementation of shock control requires an adequate adaptation of the SCB crest as a response to the ever-changing flight conditions, an actuation system based on differential pressurization of a functional surface was introduced. Furthermore, the proposed concept aims at a swift introduction into production by maintaining a conventional mechanism for the spoiler deployment which is achieved through a parallel actuation system that preserves the load-

carrying passive structure of the spoiler body.

The feasibility study corroborated the hypothesis that a compromise between design complexity and adaptability qualities can indeed be struck for a two chamber configuration. This leads to a relatively simple actuation mechanism, specially when compared to previous concepts such as the ones proposed by Wadehn et al.[10] and Bein et al.[2], which require a large number of actuators and complex control systems.

The analysis also sets the case for a chamber interface with variable stiffness as a means to improve the range of adaptability without incurring deterioration of morph quality. This can be achieved using reinforced smart laminates with embedded SMA actuators as stiffeners that permit load transfer between the laminate and actuator during activation.

References

- [1] P. Ashill et al. "A novel technique for controlling shock strength of laminar flow aerofoil sections". 1992.
- [2] T. Bein et al. "An adaptive spoiler to control the transonic shock" (2000).
- [3] G. Dargel et al. "Assessment of the Capability of Drag Reduction of the Shock Control Device "SC Bump" on Airfoil Flows and Application Aspects on Wings". 1999.
- [4] *EUROSHOCK - Drag Reduction by Passive Shock Control: Results of the Project EUROSHOCK, AER2-CT92-0049 Supported by the European Union, 1993 - 1995 (Notes on Numerical Fluid Mechanics)*. 1997.
- [5] J. C. Lagarias et al. "Convergence Properties of the Nelder-Mead Simplex Method in Low Dimensions" (1998).
- [6] H. Policarpo et al. "Using symbolic computation for teaching structural mechanics I: frames". 2012.
- [7] J. W. Smith et al. "Variable-camber systems integration and operational performance of the AFTI/F-111 mission adaptive wing". 1992.
- [8] A. Sommerer et al. "Numerical Optimization of Adaptive Transonic Airfoils with Variable Camber". 2000.
- [9] E. Stanewsky et al. *Drag Reduction by Shock and Boundary Layer Control: Results of the Project EUROSHOCK II. Supported by the European Union 1996-1999*.
- [10] W. Wadehn et al. "Structural Concepts and Aerodynamic Design of Shock Control Bumps". 2002.